Photocatalytic degradation of sulfamethoxazole with Co-CuS@TiO$_2$ heterostructures under solar light irradiation

Oumaima Mertah [b], Almudena Gómez-Avilés [a], Amine Slassi [c,d], Abdelhak Kherbeche [b,*], Carolina Belver [a], Jorge Bedia [a,*]

[a] *Chemical Engineering Department, Universidad Autónoma de Madrid, Campus Cantoblanco, E-28049 Madrid, Spain*
[b] *Laboratory of Materials, Processes, Catalysis, and Environment (LPCME), Sidi Mohamed Ben Abdellah University, Fez, Morocco*
[c] *Istituto Nanoscienze-CNR, Via Campi 213a, I-41125 Modena, Italy*
[d] *Laboratory for Chemistry of Novel Materials, University of Mons, Place du Parc 20, 7000 Mons, Belgium*

ARTICLE INFO

ABSTRACT

This work describes a successful approach to dope copper sulfide with different amounts of Co^{2+} ions and combine it with TiO$_2$ through a simple one-step hydrothermal process. Compared with the bare CuS, the synthesized Co-CuS@TiO$_2$ heterostructures promote charge transport and restrict the recombination of photoexcited electrons and holes. The intrinsic properties of Co-CuS@TiO$_2$ samples are systematically examined through experimental characterizations and density functional theory (DFT) theoretical calculations. Photocatalytic degradation tests under simulated solar light irradiation were performed using sulfamethoxazole degradation as a model emerging persistent antibiotic. The photocatalytic performance was enhanced after cobalt doping, and the heterostructure doped with 3% of Co exhibited the best degradation with an apparent rate constant of 0.0216 min^{-1}. This sample also showed a much faster settling than bare TiO$_2$, which indicates a much easier separation of the reaction media after being used. The enhancement of degradation is attributed to the increased light absorption and the more efficient charge transfer and separation. The plausible photocatalytic degradation mechanism of sulfamethoxazole was also proposed. This study presents a novel strategy to prepare potential photocatalysts for the elimination of emerging pollutants.

1. Introduction

In the last decades, there has been an increase in clinical research and production of pharmaceutical and personal care products that are worldwide provided. This spread usage can result in some environmental problems in natural aquatic systems and municipal wastewater effluents due to the presence of these compounds even at trace concentration [1]. Among the most used antibiotics, sulfamethoxazole (SMX) is a typical bacteriostatic sulfonamide used to treat urinary tract infections, toxoplasmosis, and sinusitis [2,3]. It has been widely detected in fresh/wastewater due to its extensive use, chemical stability, and low biodegradability [4]. SMX, as a refractory organic compound, cannot be efficiently removed by some conventional treatment processes [5]. The presence of SMX in wastewater, and surface and ground waters has been confirmed by previous studies [6,7]. The SMX concentration in these water matrices is in the range of nano- to micrograms per liter, even higher in hospital wastewaters [7]. As a consequence of the

scarcity of freshwaters, wastewater is usually used for irrigation, which has resulted in the detection of SMX in vegetable crops (radish leaf: 2.7 μg/kg [8], tomato: 5.26 μg/kg [9] or lettuce: 15 ng/kg [10]), with the consequent menace to the human and animal health. Therefore, it is necessary to develop sustainable and innovative technologies to prevent the accumulation of this type of emerging contaminants in natural waters. Solar photocatalysis has proved to be among the most eco-friendly and sustainable technologies for the effective treatment of antibiotic-resistant pollutants in aquatic environments [11,12]. The development of solar photocatalysts is still highly stymied due to insufficient use of sunlight and the rapid recombination of the photogenerated electron-hole pairs, resulting in low degradation efficiencies.

TiO$_2$ is one of the most used photocatalysts. However, the photocatalytic activity of TiO$_2$ is still restricted due to insufficient use of the sunlight spectrum and the rapid recombination of the photogenerated electron-hole pairs, which usually result in low degradation efficiencies under solar irradiation [13]. In addition, this low efficiency can result in

the generation of by-products that could be more toxic than the original contaminants [14]. Many different approaches have been adopted to improve the efficiency and practical applications of TiO_2 photocatalyst. The formation of a heterojunction structure or loading of a transition metal with TiO_2 can simultaneously boost the light absorption in the solar spectrum and improve the charge separation by the formation of an interfacial electric field because of band edge alignments [15]. Recently, transition metal sulfides have attracted great interest for their use as photocatalysts because of their superior optical and electronic properties and suitable bandgap potential. Copper sulfide (CuS) is a non-toxic and low-cost semiconductor. It has been widely exploited to enhance the photocatalytic performance of TiO_2 due to its great potential in using solar energy with a narrow bandgap (1.2–2.2 eV) [16]. Chen et al. [17] reported the synthesis of CuS/TiO_2 heterostructures by successive ionic layer adsorption and reaction methods. The samples facilitated the separation of photoinduced charges, which resulted in enhanced photochemical activity. Chen et al. [18] confirmed that immobilized TiO_2 nanobelts modified by Au and CuS nanoparticles retard the recombination of photogenerated electron-hole pairs, leading to a more efficient interfacial charge transfer, and consequently enhancing the photocatalytic degradation of oxytetracycline. Copper sulfide has been also combined with other semiconductors than TiO_2 looking for enhanced photoactivity under different conditions. In this sense, Chang et al. [19] obtained higher quantum yields with $Fe_3O_4@CuS/ZnS$ heterostructure due to the reduced recombination of photogenerated electrons and holes as a consequence of the electron transfer from ZnS to CuS. Song et al. [20] confirmed that the photoinduced electrons produced in WO_3 can be rapidly captured by CuS, which resulted in a much higher degradation efficiency than those of bare WO_3 and CuS. Lai et al. [21] revealed that $CuS/BiVO_4$ photocatalyst enhanced the removal efficiency of ciprofloxacin due to the effective separation of photogenerated carriers via the formation of the heterojunction.

Despite some progress, the control of the rapid recombination of photo-generated electron-hole pairs in CuS-based TiO_2 remains a challenge [17]. The doping of photocatalysts with transition-metal ions can be considered a promising strategy to enhance photocatalytic performance. Various transition metals including Cu, Ni, Co, and Cr, among others, have been successfully doped on various photocatalysts (e.g. CdS, TiO_2, $CsPbCl_3$, and $BiVO_4$) to promote the photocatalytic activity and minimize the electron-hole recombination and charge transfer at the interface. Cobalt doping has improved photocatalytic activity in several applications like degradation of organic pollutants [22], hydrogen production [23], and reduction of CO_2 [24]. Doping with Co might generate lattice distortions and defects in the semiconductor structures that facilitate the adsorption of the pollutants on the surface and act as charge traps reducing the charge recombination [25]. Hosseinpour et al. [26] reported that doping with Co^{2+} reduced the band gap values by controlling the morphology of CuS structures.

In this study, Co-doped CuS based TiO_2 heterostructures were synthesized by a simple one-step hydrothermal method. The effect of Co doping on CuS/TiO_2 heterostructure was systematically studied. The photocatalytic performance was tested in SMX degradation as a model pollutant under simulated solar light irradiation. The main benefits of this combination are a faster electron mobility, an improvement of the visible-light absorption, and a better transfer of photogenerated charge carriers during the photocatalytic degradation process. In addition, density functional theory (DFT) was used to study the interface, the transfer mechanism, and the mechanisms for the photocatalytic improvement of the heterostructures. This allows to understand the Fermi level position and to identify the reaction intermediates in the solid/liquid interface for SMX degradation.

2. Experimental section

2.1. Chemicals

The following chemicals were analytical grade (purity, >99%) and were provided from Sigma-Aldrich: Copper (II) chloride dihydrate ($CuCl_2.2H_2O$); thiourea (H_2NCSNH_2); cobalt (II) nitrate hexahydrate (Co $(NO_3)_2,6H_2O$); sulfamethoxazole (SMX, $C_{10}H_{11}N_3O_3S$); KI, *tert*- butyl alcohol (TBA) and p-benzoquinone (p-BQ). TiO_2 (P25), which contained 80% anatase and 20% rutile, was also obtained from Sigma-Aldrich. Acetonitrile (ACN, UV HPLC grade), acetic acid ($\geq$ 99%), and absolute ethanol (EtOH, 99.7%) were acquired from Scharlab. While $AgNO_3$ was provided by Alfa Aesar. Ultrapure deionized water (18.2 MΩ·cm) was used in all experiments except for pollutant solutions that were performed with deionized water (type II).

2.2. Photocatalyst synthesis

2.2.1. Synthesis of CuS
CuS was prepared in an aqueous solution using a hydrothermal method [27,28]. In a typical synthesis, 0.2 M of thiourea was dissolved in 40 mL of type I water, named solution A. At the same time, 0.16 M of copper chloride was dissolved in another 40 mL of type I water under magnetic stirring, named solution B. Then, solution A was slowly added to solution B and magnetically stirred for 2 h at room temperature. The resulting mixture was transferred into a 100 mL Teflon-lined stainless-steel autoclave and treated at 160 °C for 24 h. Subsequently, the obtained black precipitate was collected by centrifugation (3500 rpm, 5 min) and washed with ethanol and distilled water. Finally, it was dried overnight in a vacuum oven at 70 °C.

2.2.2. Synthesis of Co-CuS@TiO₂ heterostructures
Co-CuS@TiO_2 heterostructures were synthesized with different molar ratios of cobalt (1, 3 and 5%) and CuS by hydrothermal synthesis. Firstly, TiO_2 (20 wt% of the theoretical CoCuS) was dispersed in 40 mL of type I water. After that, different molar ratios of copper chloride and cobalt were dissolved in the above solution and was magnetically stirred for 1 h, followed by ultrasonication for 30 min until the solution was homogenous (solution A). Subsequently, 1.04 g of thiourea was dissolved in 40 mL of type I water at room temperature for 1 h. Solution A was added dropwise to the suspension of thiourea and was stirred for another 2 h. Then, the mixture was transferred into a Teflon-lined autoclave and kept at 160 °C for 24 h. Finally, the product was centrifuged and washed several times with ethanol and water type II to remove organic residues. The collected solid powder was dried in a vacuum oven at 70 °C overnight. The as-prepared Co-CuS@TiO_2 were denoted as CuS@TiO_2 (not doped with Co), 1%CoCuS/TiO_2, 3%CoCuS/ TiO_2, and 5%CoCuS/TiO_2 (the percentage corresponding to the Co amount).

2.3. Characterization

The X-ray diffractometer (XRD, Bruker D8 Discover) equipped with a Cu Kα radiation source (λ = 0.154 nm) was used to analyze the crystalline structure of the samples in the 2θ range from 10 to 70° under a scanning rate of 5°·min⁻¹. Scanning electron microscopy (SEM; HITACHI S-4800) with energy-dispersive X-ray spectroscopy (EDX) was used to observe the surface morphology and structure of the particles. N_2 adsorption-desorption isotherms at −196 °C were obtained in a TriStar 123 equipment (Micromeritics II 3020) to determine the textural properties. Each sample was outgassed at 120 °C for 12 h before measurement under vacuum (VacPrep 60, Micromeritics). The total surface area (S_{BET}) was estimated using the Brunauer-Emmett-Teller (BET) method [29]. The total pore volume (V_T) was calculated from the amount of adsorbed nitrogen at a relative pressure of $P/P_0 = 0.99$. UV–visible diffuse reflectance spectroscopy (UV–vis DRS, Shimadzu UV2600) was

acquired in the wavelength range of 200–800 nm using $BaSO_4$ as the reflectance standard. The bandgap energy (Eg) of semiconductors was estimated using the Tauc plot method [30], considering the photocatalysts as indirect semiconductors. Settling tests were performed as an indication of the ease of separation of the photocatalysts from the treated streams using a UV–vis spectrophotometer (Shimadzu UV2600) [31]. To determine the settling speed of the photocatalyst, the time evolution of the absorbance at 600 nm of catalyst suspensions ($1 \ g \cdot L^{-1}$) was measured continuously in a quartz cuvette for 4 h. The solution was shaken for 60 s before starting the measurement. Metrohm Autolab potentiostat equipment (PGSTAT204) was used to determine the electrochemical properties of the different materials. This system comprises an indium tin oxide (DropSens ITO10) working electrode, with counter and reference counterparts of carbon and silver electrodes, respectively [32,33]. The materials suspensions ($1 \ mg \cdot mL^{-1}$) were prepared in 0.1 M Na_2SO_4 (pH ~ 4.5 at 25 °C) and placed into the electrochemical cell. Electrochemical impedance spectroscopy (EIS) was registered by scanning the frequency range from 10^5 to 10^{-1} Hz at a fixed potential of -1.2 V, whereas Mott-Schottky (M-S) plots were obtained applying a voltage between -1.5 and 0.4 V under a constant frequency of 100 Hz. The flat band potential of the material, V_{fb}, was obtained following Mott–Schottky equation (Eq. (1)) [34]:

$$\frac{1}{C^2} = \frac{2}{\varepsilon \cdot \varepsilon_0 \cdot e \cdot N_D} \cdot \left(V - V_{fb} - \frac{k \cdot T}{e} \right), \tag{1}$$

being C the capacitance of the semiconductor-electrolyte junction at applied voltage V; ε and ε_0 the permittivity of the semiconductor and the void, respectively; e the electron charge; k the Boltzmann's constant; and T the temperature. V_{fb} is estimated from the intercept point of the tangent line with the potential axis in the plot of $1/C^2$ vs V. The potential of the conduction band (V_{CB}) can be calculated with respect to the normal hydrogen electrode (NHE) at pH 7 following a Nernstian shift using Eq. (2) [35]:

$$V_{CB} = V_{fb(Ag/AgCl,pH)} + \Delta V_{(Ag/AgCl,NHE)} - 0.059 \cdot (7 - pH), \tag{2}$$

where $\Delta V_{(Ag/AgCl, NHE)}$ is the Ag/AgCl potential against NHE (0.21 V). Finally, the valence band potential (V_{VB}) can be estimated following Eq. (3):

$$V_{VB} = V_{CB} + E_g / e, \tag{3}$$

where E_g is the bandgap of the semiconductor.

2.4. Photocatalytic test

Sulfamethoxazole (SMX) degradation experiments were performed using a simulated solar radiation reactor (Suntest XLS+ simulator, ATLAS) equipped with a Xenon lamp emitting $600 \ W \cdot m^{-2}$ and a light correction filter $\lambda \leq 290$ nm. Briefly, the as-prepared photocatalysts ($250 \ mg \cdot L^{-1}$) were suspended in 150 mL of SMZ solution in deionized water (type II; $5 \ mg \cdot L^{-1}$) in a Pyrex jacketed closed reactor at a controlled temperature (25 °C). Before turning on the simulated solar light, the dispersion was magnetically stirred in dark for 60 min to ensure the stable adsorption-desorption equilibrium between the photocatalyst and SMX. Afterward, the lamp was turned on and the photocatalytic experiment was carried out for 6 h. During each photocatalytic experiment, at different irradiation times, about 500 μL of the solution was collected and filtered using 0.2 μm syringeless filters (Scharlab) to separate the photocatalyst. For comparison, the photolysis experiment was performed under the same conditions in the absence of the photocatalyst to check the stability of the pollutant under irradiation. Filtered samples were analyzed to determine the SMX concentration in the solution using a High-Performance Liquid Chromatography (HPLC; Shimadzu Prominence-I LC-2030C) equipped with a C18-column (Eclipse Plus 5 μm, Agilent) and a Diode Array detector type SPD-M30A. An isocratic method (70/30%) of a mixture of 0.1% *v/v* acetic acid and

acetonitrile were used as a mobile phase at a flow rate of $0.8 \ mL \cdot min^{-1}$ at 35 °C. The maximum absorption wavelength for SMX detection was set at 268 nm.

Quenching experiments were carried out with $AgNO_3$, KI, *tert*-butyl alcohol (TBA), and *p*-benzoquinone (*p*-BQ). $AgNO_3$ (1 mM) was used as scavenger of the photogenerated electrons, while KI (1 mM) was considered as a hole scavenger. In the case of *Tert*-butyl alcohol (TBA, 3.3 mM) is used as an effective scavenger for hydroxyl radicals ($HO^\bullet$) [36], though *p*-benzoquinone (p-BQ, 3.3 mM) is used as superoxide radicals ($O_2^{\bullet-}$) scavenger. These experiments were performed under the same reaction conditions described above just adding the scavenger to the SMX solution after the dark adsorption equilibrium step.

2.5. Computational details

The theoretical calculations were carried out within the density functional theory (DFT) formalism as implemented in the Vienna ab initio simulation package (VASP) with the projector-augmented wave (PAW) for a basis set [37]. The generalized gradient approximation (GGA) according to Perdew−Burke−Ernzerhof (PBE) was used to trait the exchange and correlation contribution [38]. The weak van der Waals (vdW) interactions were considered by including the Grimme dispersion correction of the DFT-2D method [39]. A kinetic energy cutoff of 450 eV and a Γ-centered $3 \times 3 \times 1$ k-point grid for the Brillouin zone integrations were used. The heterostructure models were constructed by placing rectangular unit cells of CuS (110) on a rectangular unit cell of TiO_2 (101) with an interfacial surface area of a = 20.29 and b = 15.82 Å. The used heterostructure models consisted of 564 atoms, including 90 S, 90 Cu, 256 O, and 128 Ti atoms. Co-doping was introduced by substituting a Cu atom with a Co dopant at the interface, resulting in a representative doping concentration of 1.12%.

3. Results and discussion

3.1. Characterization

Fig. 1 represents the XRD patterns CuS, CuS/TiO_2, and Co-CuS@TiO_2 samples. That of copper sulfide indicates a high crystallinity and the confirms the formation of CuS hexagonal covellite phase (JCPDS card N° 06–0464) with space group (P63/mmc), indexed as 2θ (hkl) = 27.1° (100), 27.6° (101), 29.2° (102), 31.8° (103), 32.8° (006), 38.8° (105), 47.9° (110), 52.7° (108) and 59.3° (116) [19,40]. The XRD pattern illustrates two peaks observed at 2θ of 32.2 and 46.2°, indicating the formation of intermediate cubic digenite ($Cu_{1.8}S$, JCPDS card N° 23–0960) phase [41]. The XRD pattern of TiO_2 shows the typical diffraction peaks of tetragonal anatase and rutile phases in P25. The characteristic peaks are related to the presence of the anatase phase of TiO_2 (JCPDS card N° 21–1272, 78–2486) at 25.6, 38.3, 48.4, 63.0 and 69.3° ascribed to (101), (004), (200), (204) and (116) reflections, respectively. And the characteristic peaks related to the tetragonal rutile phase (JCPDS card N° 21–1276) at 27.7, 36.2, 41.6, 54.6, and 56.6° typical of the reflections of the crystal planes (110), (101), (111), (211) and (220), respectively. The XRD patterns of $CoCuS/TiO_2$ heterostructures show the characteristic peaks of both CuS (only hexagonal covellite phase) and TiO_2, which seems to suggest the coexistence of both phases in the heterostructure. All the peaks are of relatively high intensity, which indicates a high crystallinity of the as-synthesized samples [18]. There are no additional characteristic peaks for cobalt or sulfide-based crystalline impurities such as cobalt sulfide, although it should be considered that XRD would not have enough sensitivity to detect so low amount of Co impurities. In addition, the increase of the Co dopant concentration does not seem to significantly modify the diffraction patterns. This suggests a successful substitution of Co ions in the regular lattice site of CuS to form Co-CuS@TiO_2, probably due to the very similar ionic radius of Co^{2+} (0.72 Å) and Cu^{2+} (0.73 Å).
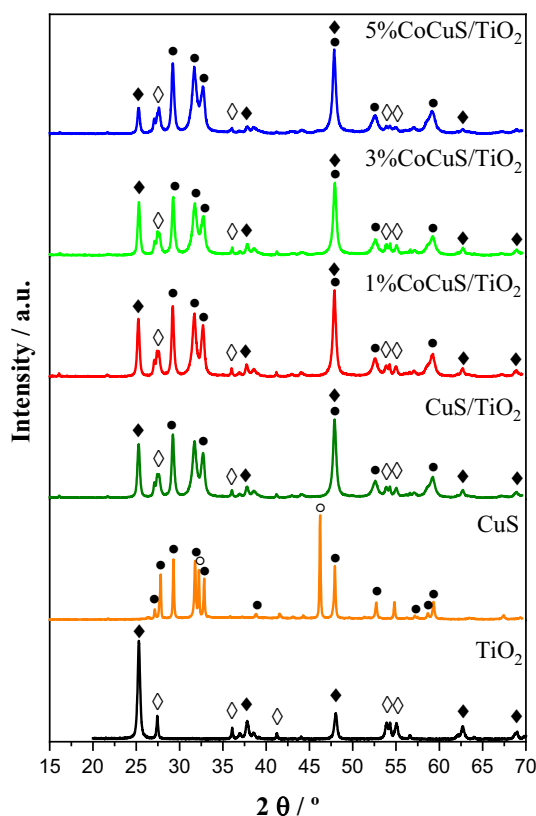
Fig. 2 represents the FTIR spectrum of 3%CoCuS/TiO_2. The broad

Fig. 1. XRD patterns: ◆ Anatase tetragonal (JCPDS 78–2486; JCPDS 21–1272); ◇ Rutile tetragonal (JCPDS 21–1276); ● CuS (JCPDS 06–0464); ○ intermediate cubic digenite, $Cu_{1.8}S$ (JCPDS 23–0960).
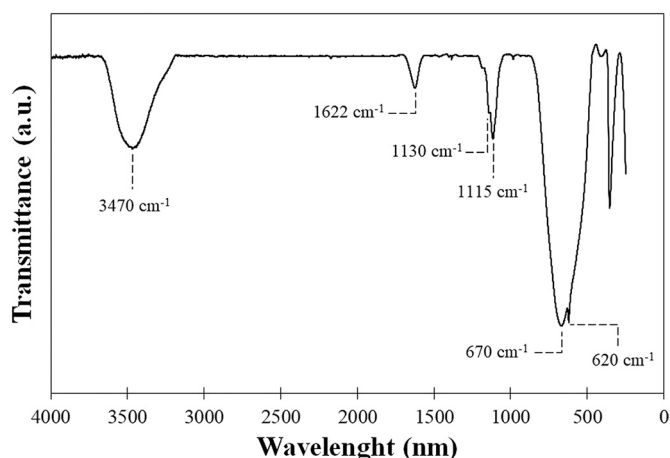

Fig. 2. FTIR spectrum of 3%CoCuS/TiO$_2$ catalyst.

band is centered at ca. 3470 cm^{-1} and covering the range of 3200–3500 cm^{-1} is attributed to the stretching mode of the hydroxyl ions, while the band at 1635 cm^{-1} corresponds to the bending modes of H–O–H moieties of absorbed water, which indicates that the existing water molecules are absorbed by sulfide products. The bands at 620 and 670 cm^{-1} (symmetrical stretch) and 1115 and 1130 cm^{-1} (asymmetrical stretch) correspond to the Cu—S or Co—S vibrations, which are overlapped with the vibrations of the Ti-O-Ti bonds due to the presence of TiO$_2$ in the heterostructure. This FTIR spectrum supports the successful synthesis of the 3%CoCuS/TiO$_2$ catalyst.

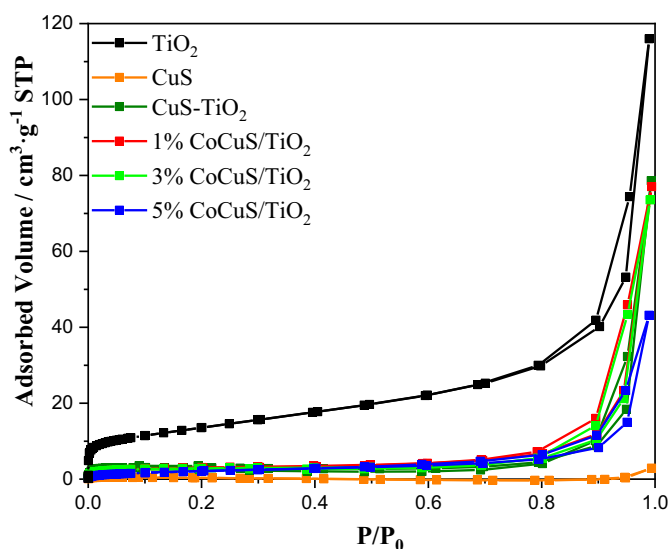Fig. 3 shows the nitrogen adsorption-desorption isotherms at −196 °C of TiO$_2$, CuS, CuS/TiO$_2$, and Co-CuS@TiO$_2$ heterostructures.

Fig. 3. N$_2$ adsorption-desorption isotherms at −196 °C.

All isotherms are classic type IV according to the International Union of Pure and Applied Chemistry (IUPAC) classification accompanied by remarkable H3 hysteresis loops, indicating the predominantly existence of mesoporous structures successfully constructed by the aggregation of microparticles [42,43]. The highest amount of adsorbed N$_2$ corresponds to TiO$_2$ and the lowest one to CuS, with all the combined heterostructures with intermediate adsorbed amounts. All the isotherms of the samples containing TiO$_2$ exhibited H3 hysteresis loops at higher relative pressure, which confirmed the presence of a certain amount of mesopores. The type H3 hysteresis loops are characteristic of narrow slit-shaped pores. Table 1 summarizes the porous texture parameters obtained from the isotherms. TiO$_2$ has a relatively large specific surface area of 49 m$^2 \cdot$g^{-1}, while pure CuS does not exhibit a specific surface area due to its almost negligible N$_2$ adsorption. The combination of the TiO$_2$ with CuS results in very similar adsorption isotherms, and consequently, very similar porous texture parameters regardless of the amount of Co. Only a significant reduction of the total pore volume is observed when the amount of Co-doped reaches 5%.

Fig. 4A and B are SEM micrographs of CuS and 3%CoCuS/TiO$_2$, respectively. Fig. 4A shows that CuS consists of agglomerated particles having intersected sheets with irregular shapes [44]. The addition of Co and TiO$_2$ (Fig. 4B) results in the Co-doped CuS sheets spotted with TiO$_2$ nanoparticles of irregular morphology. In addition, the CuS sheets decreased their particle size, which suggests that TiO$_2$ can inhibit the growth of CuS sheets during the hydrothermal treatment [45]. The energy dispersive spectrum (EDS) of 3%CoCuS/TiO$_2$ (Fig. 4C) confirmed the presence of Cu, S, Co, Ti, and O in the heterostructure. The atomic ratio of Cu:S is approximately 1:1 (inset table in C), which is consistent with the stoichiometric ratio of CoCuS, and the same happens with the atomic ratios of Ti:O that are 1:2 in agreement with the TiO$_2$

Table 1
Porous texture parameters and band gap values (Eg).

Samples	S$_{BET}$ [a] (m$^2 \cdot$g^{-1})	V$_{total}$ [b] (cm$^3 \cdot$g^{-1})	Band Gap (eV)
TiO$_2$	49	0.179	3.3
CuS	–	–	1.6
CuS/TiO$_2$	9	0.122	3.2
1%CoCuS/TiO$_2$	10	0.120	3.4
3%CoCuS/TiO$_2$	9	0.114	3.4
5%CoCuS/TiO$_2$	8	0.067	3.5

[a] Specific surface area.
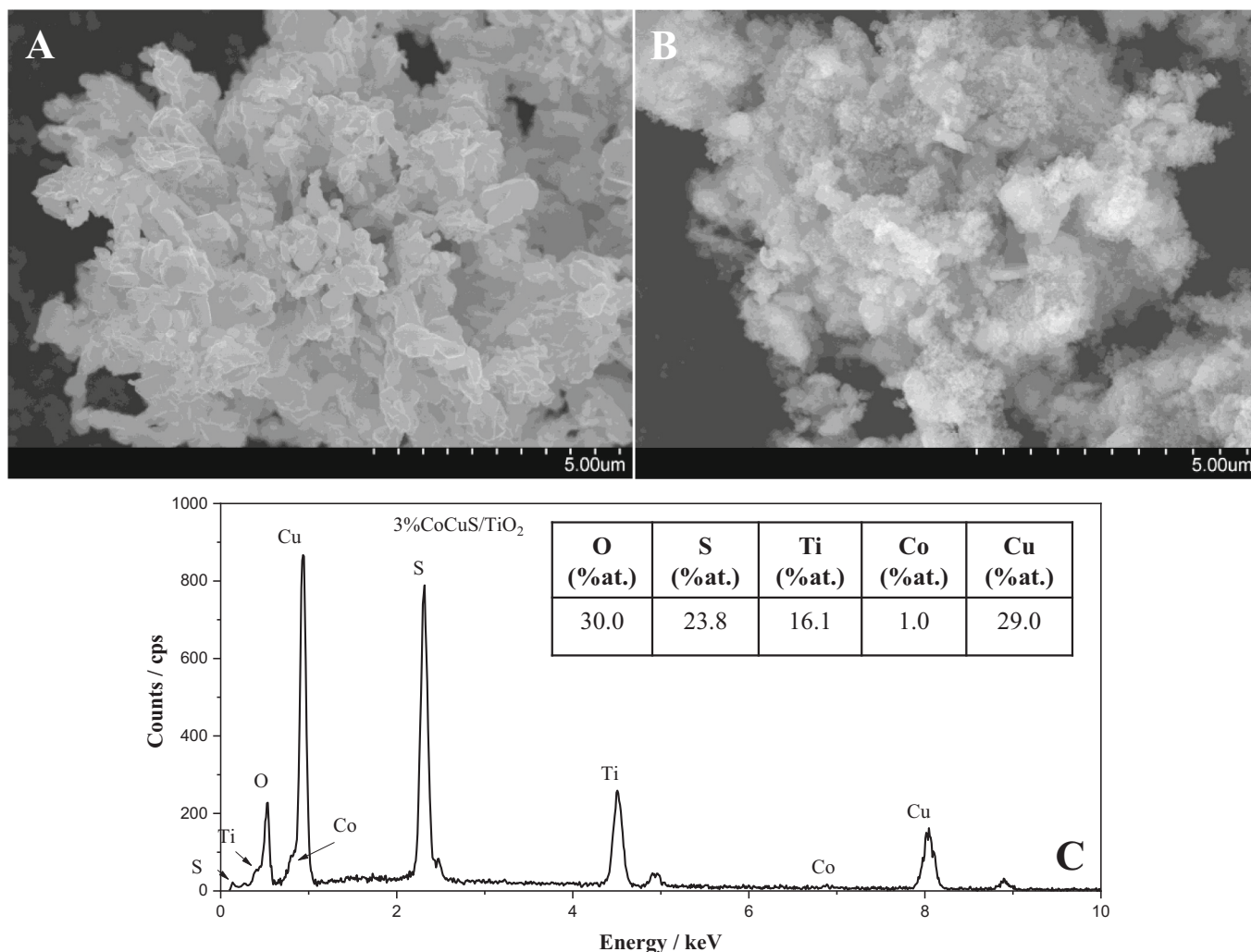[b] Total pore volume.

Fig. 4. SEM images of A) CuS, B) 3%CoCuS/TiO$_2$ and C) EDX pattern of 3%CoCuS/TiO$_2$.

formulation. Based on these values, the CoCuS: TiO$_2$ mass ratio in the heterostructure is close to 0.32. The conversion of the EDS values from atomic to mass concentration reveals that the real content of TiO$_2$ in the catalysts is ca. 32%, which agrees with the theoretical 20% used in the synthesis, considering a reasonable yield of the Co-CuS synthesis process. These results support the successful synthesis of the TiO$_2$ plus Co-doped CuS heterostructure.

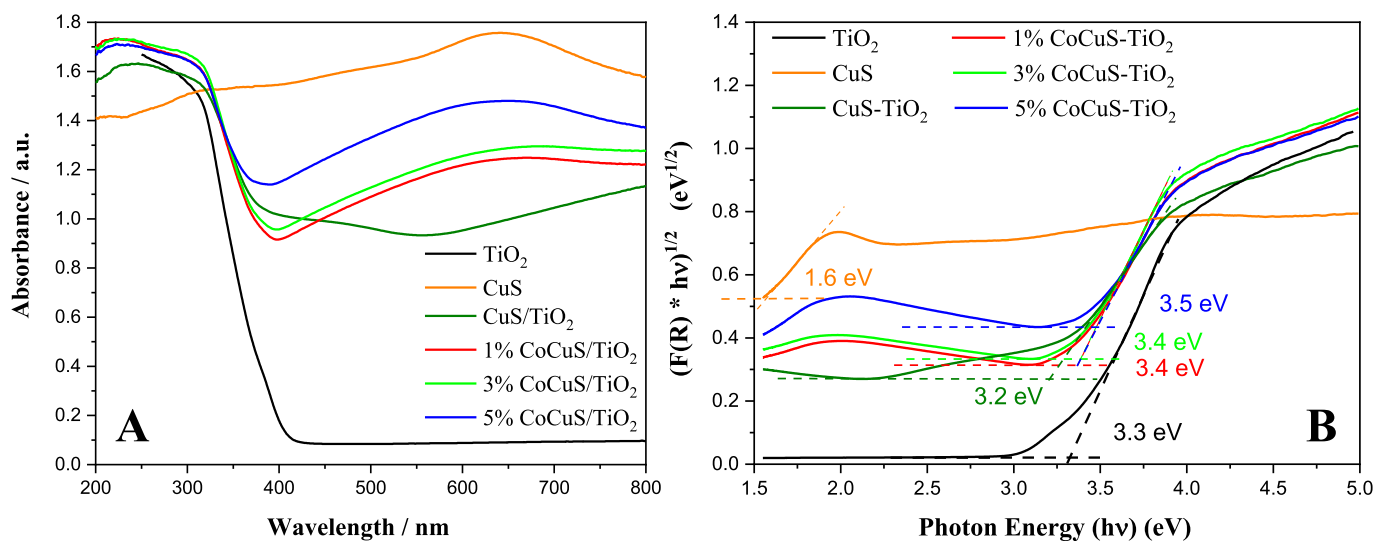Fig. 5A represents the UV–vis diffuse reflectance spectra (DRS).

Fig. 5. UV–visible diffuse absorbance spectra (A) and Tauc plots (B).

Pristine CuS displays the strongest wavelength absorption edge in the visible-light region (between 600 and 700 nm) as a consequence of its narrow bandgap energy and electron inter-band excited transition [46]. By contrast, TiO_2 exhibits strong absorption in the ultraviolet region (below 400 nm) attributed to the band-to-band transition [47,48]. The combination of CuS with TiO_2 shows stronger absorption intensity than neat TiO_2 in the visible light region, which can subsequently result in a better photocatalytic behavior under solar light illumination. Moreover, with the introduction and the increase of the Co concentration, the absorption edges display a gradual red-shift and enhanced absorbance in the visible light region [26]. The formation of Co-CuS@TiO_2 heterostructures would positively influence the photophysical characteristics of the as-prepared samples. Furthermore, Fig. 5B represents the Tauc plots used for the calculation of the bandgap energies of the different samples considering them as indirect semiconductors (like the bare TiO_2) [49]. CuS band gap was 1.6 eV in agreement with previous studies [46,50]. The values of the heterostructures are slightly higher than that of pure TiO_2 (3.3 eV) [51], indicating that the interaction with CuS does not modify significantly the TiO_2 band gap in any case.

3.2. Photocatalytic degradation of SMX

The photocatalytic performance of the samples was assessed in the degradation of sulfamethoxazole (SMX) under simulated solar light irradiation. The SMX adsorption in dark was negligible in all cases. Fig. 6A represents the SMX evolution with the irradiation time of the different samples. In the absence of photocatalyst, the SMX photodegradation was very low, close to 10% after 6 h. Co-CuS@TiO_2 heterostructures improve the rate of SMX removal over that observed with raw CuS and CuS/TiO_2. This improvement can be attributed to the superior light absorption under the excitation of visible light, although lower recombination of photo-induced e^-/h^+ pairs and/or a better charge mobility cannot be discarded. 1% and 3%CoCuS/TiO_2 achieved a complete SMX degradation after 120 min. TiO_2 displays a slightly faster degradation than Co-CuS@TiO_2 heterostructures, with complete SMX degradation in <100 min. It is well-known that the photocatalytic activity is highly influenced by the particle size [52], which could explain the better performance of TiO_2 due to its very low particle size. However, this low particle size results also in a much more difficult separation of the reaction media after use, which could justify the best behavior of the Co-CuS@TiO_2 heterostructures despite their slightly

lower photoactivity as we will prove below. SMX degradation kinetics were fitted by the pseudo-first-order kinetic reaction using the Langmuir-Hinshelwood model [53], as expressed in Eq. (4):

$$Ln\left(\frac{C}{C_0}\right) = -K_{app} \cdot t \tag{4}$$

where K_{app} (min^{-1}) is the apparent reaction rate constant, C_0 and C are the SMX initial concentration (5 mg·L^{-1}), and the concentration of SMX at reaction time t, respectively. Fig. 6B summarizes the values of the apparent pseudo-first-order rate constants with the different photocatalysts. The rate constant obtained by the 3%CoCuS/TiO_2 heterostructure (0.0216 min^{-1}) was remarkably higher than that achieved by CuS (0.0004 min^{-1}), 1%CoCuS/TiO_2 (0.0187 min^{-1}), and 5%CoCuS/TiO_2 (0.0107 min^{-1}). It seems that the anchoring Co on the surface of CuS and TiO_2 can promote their photocatalytic performances. Moreover, the chemical bonds formed between them could easily allow the transfer of photogenerated carriers, reducing their recombination, which leads to better performance and stability in photocatalytic reactions [54]. The highest kinetic rate was achieved using TiO_2 (0.0535 min^{-1}) but, as aforementioned, the photoactivity is not the only characteristic that influences the interest of a photocatalyst. The separation of photocatalyst from the media after the application is a crucial aspect of the implementation in real applications. In this sense, Fig. 7 represents the light absorbance evolution at 600 nm with time during a settling test performed in a UV–Vis cell with 3%CoCuS/TiO_2 and TiO_2 suspensions (1 g·L^{-1}). With this procedure, we can evaluate the settling ability of TiO_2 and 3%CoCuS/TiO_2 in water closely related to their separation performance. As can be observed, TiO_2 particles are hardly settled even after 4 h, while 3%CoCuS/TiO_2 was almost completely settled after only 30 min. This is most likely due to the bigger particle size of 3%CoCuS/TiO_2 than TiO_2, which greatly facilitates enormously the separation of the photocatalysts from the treated solution after use. Therefore, 3%CoCuS/TiO_2 seems to be suitable in real applications to overcome the limitation of suspended material, especially the difficulty of separation and high turbidity in an aqueous solution.

In order to confirm the stability of the catalyst under the reaction conditions, 3%CoCuS/TiO_2 sample was submitted to use in several reaction cycles. After each cycle, the catalyst was recovered by filtration, rinsed with distilled water, and dried prior to use in the next reaction cycle. Fig. 8 represents the SMX conversion after 3 h of irradiation in each cycle. It can be concluded that 3%CoCuS/TiO_2 sample is fairly
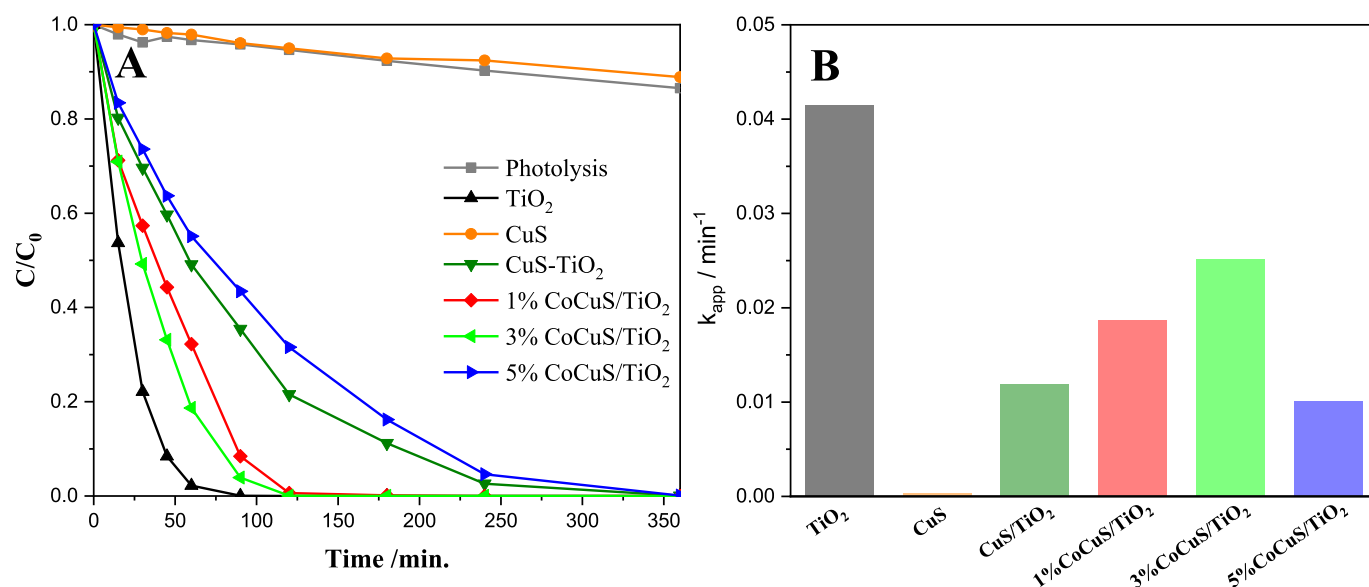

Fig. 6. (A) Time-course evolution of SMX under simulated solar light (TiO_2 dosage: 50 mg·L^{-1}; Rest photocatalyst dosage: 250 mg·L^{-1}; $[SMX]_0$: 5 mg·L^{-1}; Intensity: 600 W·m^{-2}); (B) Apparent first order rate constants.
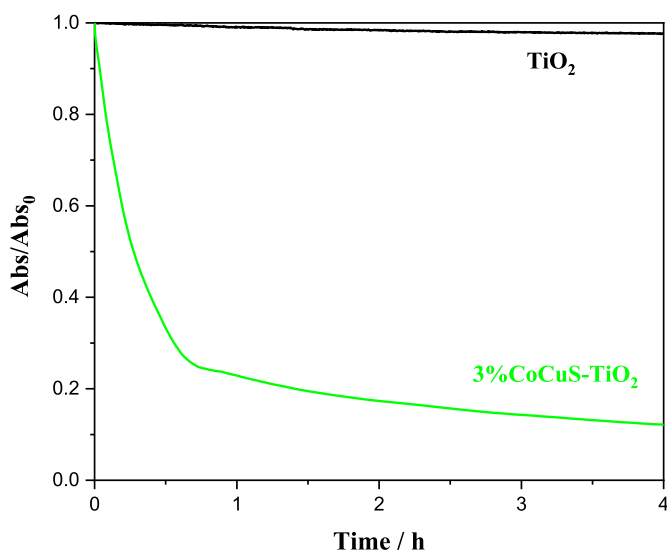
Fig. 7. Absorbance evolution profiles (600 nm) during settling test of 3% CoCuS/TiO$_2$ and TiO$_2$ suspensions (1 g·L^{-1}).
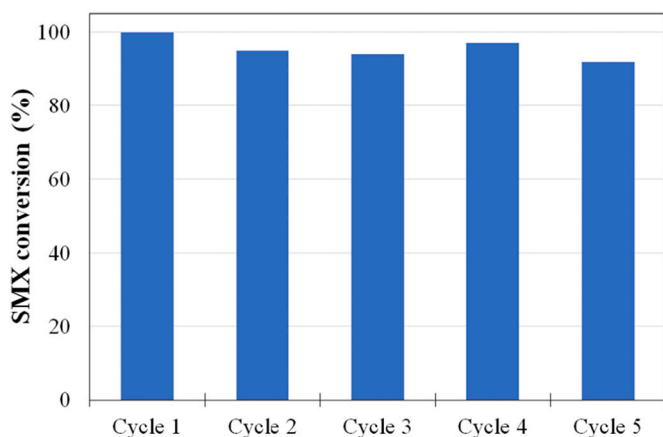

Fig. 8. SMX conversion with 3%CoCuS/TiO$_2$ after 3 h of irradiation in each cycle (Catalyst load: 250 mg·L^{-1}; [SMX]$_0$: 5 mg·L^{-1}; Intensity: 600 W·m^{-2}).

stable under the tested reaction conditions, with an almost negligible loss of activity even after 5 consecutive reaction cycles.

Quenching experiments were performed with different scavengers to evaluate the role of the different reactive oxygen species (ROS) in the SMX degradation using 3%CoCuS/TiO$_2$ under simulated solar light. The time-course evolution of SMX concentration with different scavengers (AgNO$_3$, KI, TBA, and p-BQ) was represented in Fig. 9A, while Fig. 9B exhibits the apparent first-order reaction kinetic constants of those tests. The degradation of SMX was almost completely inhibited in the presence of KI (k = 0.00024 min^{-1}), which indicates the determinant role of holes (h$^+$) formed on the 3%CoCuS/TiO$_2$ system. To a lesser extent, the degradation of SMX was significantly affected when p-BQ (k = 0.012 min^{-1}) was added to the reaction system, indicating that the superoxide radicals, O$_2^{•-}$, also slightly contributed to the degradation of SMX. On the other hand, AgNO$_3$ and TBA had a lower effect on the degradation of SMX (k = 0.016 and 0.014 min^{-1}, respectively), which indicated a minor contribution of photoelectrons and HO$^•$ radicals in the degradation process.

Electrochemical characterization was also assessed to rationalize the causes of the better photocatalytic activity of 3%CoCuS/TiO$_2$. The charge transfer resistance has been analyzed by EIS through the Nyquist plots, which are represented in Fig. 10A. 3%CoCuS/TiO$_2$ shows the

smallest arc radius, which means that it has the lowest charge transfer resistance, and consequently the best charge mobility [55,56]. This results in more available photo-induced carriers that can participate in redox reactions per unit time, thereby enhancing photocatalytic activity and justifying the best photoactivity of this catalysis. Fig. 10B displays the Mott-Schottky plots of TiO$_2$ and CuS. The positive slopes of the plots confirm that both materials act as *n*-type semiconductors [57,58]. From the intercepts of the extrapolated lines, the flat band potentials (V$_{fb}$) of TiO$_2$ and CuS can be estimated at −0.73 V for both. Using Eq. (2), the positions of the conduction bands, V_{CB}, of each material were determined to be at −0.53 and − 0.51 V, respectively. Finally, Eq. (3) allows to obtain the valence band positions, V_{VB}, considering the bandgap values, E_g, of each material (Table 1).

Considering the above results and the band edge positions of TiO$_2$ and CuS previously calculated, Fig. 11 represents a plausible degradation mechanism related to the formation of a *n-n* heterojunction between TiO$_2$ and Co-doped CuS. Based on the results of characterization and photocatalytic experiments, the main keys for high SMX degradation using Co-CuS@TiO$_2$ were the improved light absorption ability and lower charge transfer resistance. The overlapping of the conduction bands of TiO$_2$ and Co-CuS (−0.53 and − 0.51 V, respectively) in Co-CuS@TiO$_2$ heterostructure facilitates the transfer and separation of generated photo-induced electrons (e$^-$) and holes (h$^+$) [17]. After contact the Fermi levels of both semiconductors equilibrate, and an internal electric field is formed. Since, Co-CuS has a significantly narrower band gap, the electron and holes are preferably generated in this moiety. The electric field promotes the separation of the charge due to the transfer of the electrons from the CB of Co-CuS to the CV of TiO$_2$ decreasing the charge e$^-$/h$^+$ recombination [59]. The electrons accumulated in the CB of TiO$_2$ can be trapped by oxygen molecules (O$_2$) adsorbed on the TiO$_2$ surface to form $^•$O$_2^-$ [60,61], which subsequently oxidize the SMX molecules. In addition, the holes that accumulate on the VB of Co-CuS (unable to recombine due to the aforementioned transfer of electrons from the CB of Co-CuS to the CV of TiO$_2$) can directly oxidize the SMX molecules [62]. This contribution of h$^+$ and $^•$O$_2^-$ radical to the oxidation reaction is in agreement with the results observed in the scavenger tests (Fig. 9).

To in-depth understand the enhancement in the photocatalytic degradation of SMX on TiO$_2$/CuS heterostructure upon the incorporation of a Co doping, we performed density functional theory (DFT) calculations (Fig. 12). It focuses on the facet orientations of TiO$_2$(101) and CuS(110) surfaces since they are the most exposed facts observed in XRD measurements (Fig. 1). Note that, the previous density function calculations also demonstrated that CuS(110) has the lower surface energy [63]. The binding energy between the two components was calculated by the following Eq. (5):

$$E_b = \frac{E_{tot} - E_{TiO2} - E_{CuS}}{S} \tag{5}$$

Where the E$_{tot}$ is the total energy of interacted heterostructures, E$_{TiO2}$ and E$_{CuS}$ are the total energies of individual components, and S is the surface area of interfaces. The binding energy for pure heterostructure was calculated to be −14 meV·Å^{-2} and the interlayer distance to be 2.5 Å. These values indicate that the TiO$_2$(101) component strongly interacts with CuS(110) through a chemical bond [64,65]. Upon incorporating a Co dopant, the binding energy increases to −17 meV·Å^{-2} (by ~17%) and the interlayer distance decreases to 2.46 Å (by ~1.6%). This is rationalized by the increase in the amount of interfacial charge transfer, which in turn strengthens the Coulomb attraction between TiO$_2$(101) and Co-doped CuS(110) components. The amount of interfacial charge transfer was quantified by using the Bader charge analysis. In general, the computed interfacial charge transferred from CuS(110) to TiO$_2$(101) component was estimated to be 0.52 |e|·Å^{-2} upon incorporating a Co-dopant, which is higher than that for the pure case (0.46 |e|·Å^{-2}).

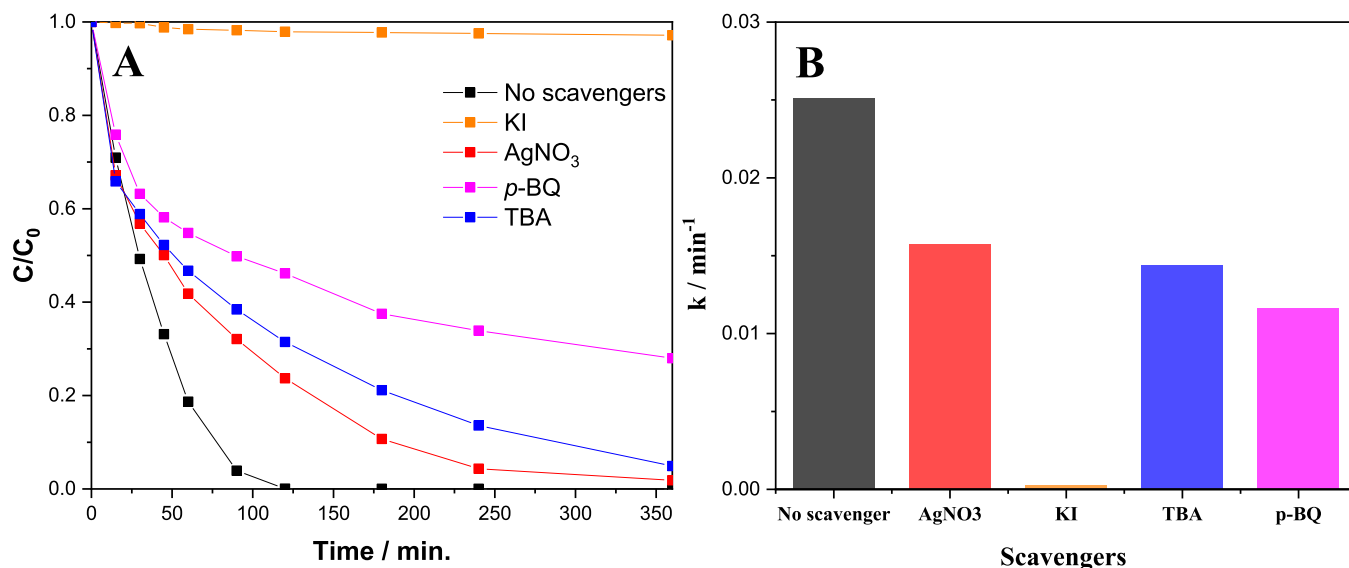The charge rearrangement at the interface due to charge transfer is

Fig. 9. (A) Effect of radical scavengers on SMX degradation using 3%CoCuS/TiO$_2$, and (B) values of the pseudo-first order rate constant of SMX disappearance (Photocatalyst dosage: 250 mg·L^{-1}; [SMX]$_0$: 5 mg·L^{-1}; Intensity: 600 W·m^{-2}).
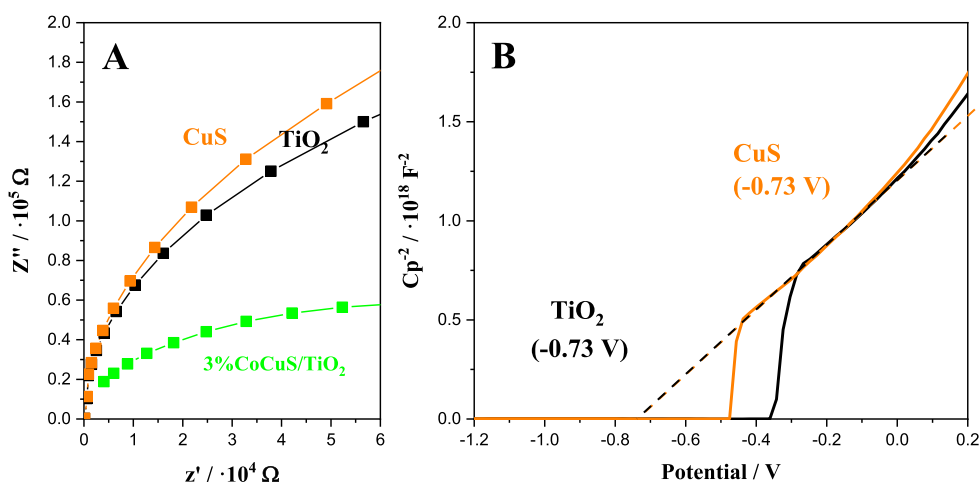

Fig. 10. (A) EIS Nyquist plots of TiO$_2$, CuS, and 3%CoCuS/TiO$_2$ and (B) Mott-Schottky plots of TiO$_2$ and CuS.

analyzed by computing the two (2D) ad three(3D)-dimensional charge density difference, defined as the subtraction of the electronic charge of a CuS/TiO$_2$ heterostructure from those of the TiO$_2$ and CuS structures as shown in Fig. 12. There is a significant charge redistribution close to the interface region, while no charge redistribution is observed far away from the interface region. Interesting, there is an accumulation of an electron spot at the TiO$_2$(101) component and a hole spot at the CuS (110) component (in agreement with the proposed photodegradation mechanism, Fig. 11), which thus establishes an interfacial dipole moment. Of note, engineering such interfacial dipole has been proved to be an effective way to improve the separation of the photogenerated hole–electron pairs [66–68]. For the sake of comparison, the charge redistribution is more noticeable upon the incorporation of Co-dopant as compared to pure heterostructure. Hence, such charge distribution at the interface promotes the formation of highly active interfacial catalytic sites for the SMX degradation process. By numerically integrating the planar-average density charge difference ($\Delta(z)$) along the z-direction (normal to the interface), we estimated the amount value of the dipole moment at the interface using the Poisson equation [69]. The calculated

dipole moment for pure heterostructure is found to be 0.47 exÅ pointing from TiO$_2$ to CuS component, whereas its magnitude increases to 0.65 exÅ upon introducing a Co-dopant. The formation of a permanent dipole moment at the interface is considered a driving force for spatial photogenerated charge separation and an increase in its magnitude is an additional value for enhancing the rate of the photogenerated electron-hole carriers participating in the photocatalytic SMX degradation.

4. Conclusions

Co-CuS@TiO$_2$ n–n heterostructures with different Co percentages have been successfully prepared by a simple hydrothermal method. The heterostructure photocatalytic behavior was analyzed by detailed characterizations, experimental tests and DFT theoretical calculation. The combination of Co-doped CuS with TiO$_2$ resulted in an improvement of the photocatalytic performance in the SMX degradation under simulated solar light and good settling ability. Such enhancement of photocatalytic activity can be assigned to the enhanced visible light-harvesting ability as well as the better transfer and separation of e$^-$/
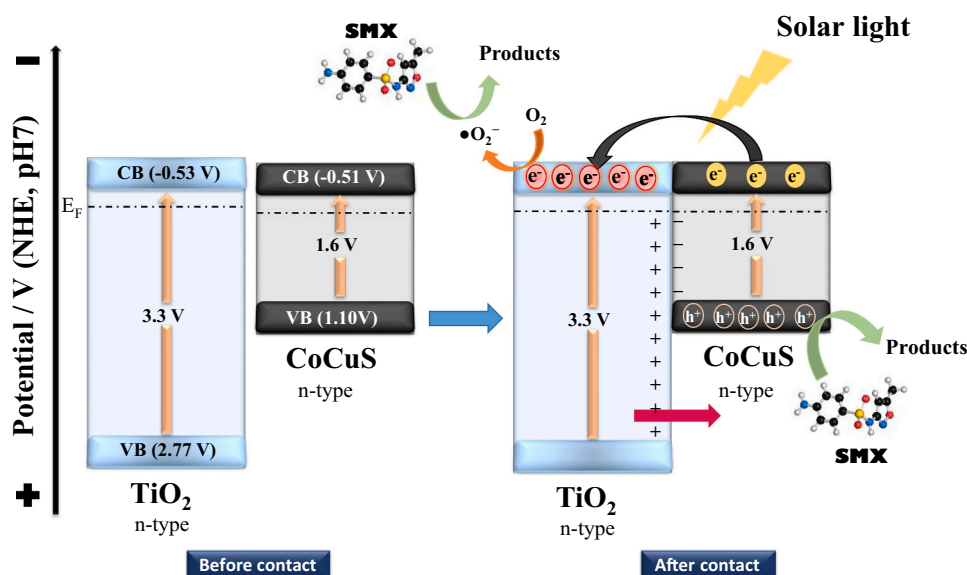
Fig. 11. Schematic illustration of the photocatalytic mechanism for Co-CuS@TiO₂ heterostructures under simulated solar light irradiation.
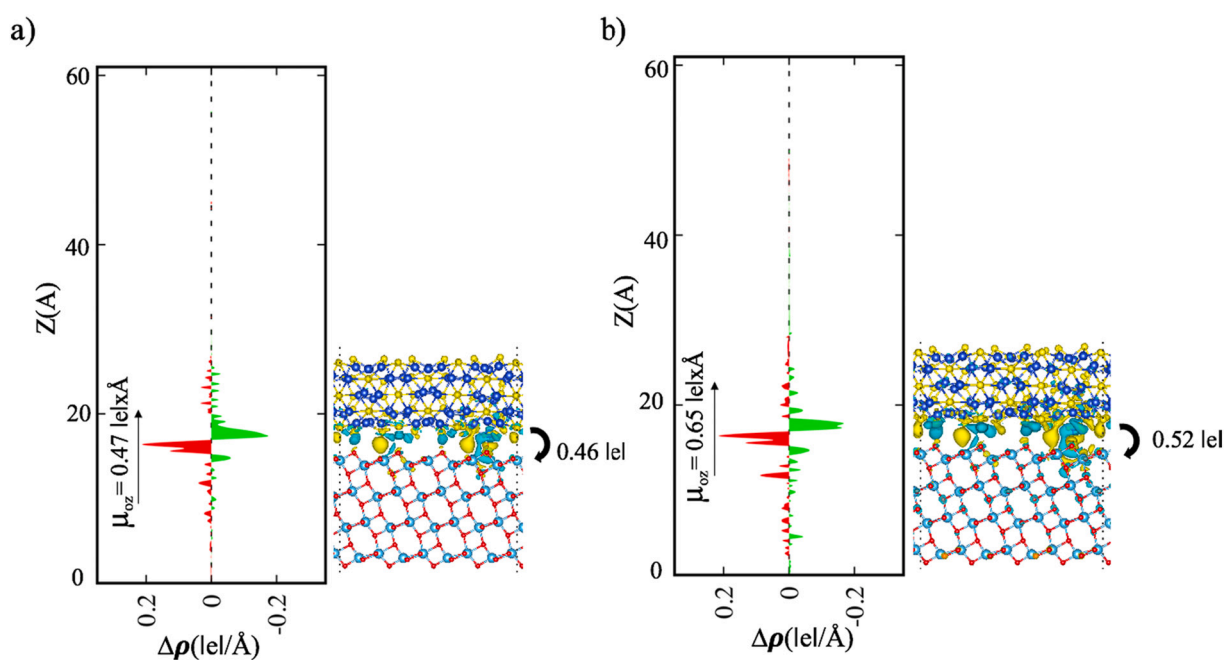

Fig. 12. Planar-averaged (2D) and three (3D)-dimensional charge difference of (A) pure CuS(110)/TiO₂(101) and (B) CoCuS(110)/TiO₂(101) heterostructures. Yellow and Cyan spots denote the depletion and accumulation of charge with an isosurface of 0.0005 e·Å⁻³. (For interpretation of the references to colour in this figure legend, the reader is referred to the web version of this article.)

h^+ pairs. The 3%CoCuS/TiO₂ sample exhibited better SMX degradation among the heterostructures. The photocatalytic mechanisms of SMX degradation are discussed in detail, being superoxide radicals, and mainly holes, the species responsible of the photodegradation of the SMX molecules. Eventually, this work would provide new insights into the development of an economical and facile path to synthesize Co-CuS/TiO₂ heterostructures as a promising choice to apply in environmental applications.

Credit author statement

Conceptualization, A.K., A.S., C.B. and J.B.; methodology, A.G.-A.

and O.M.; writing - original draft, A.G.-A. and O.M; writing - review & editing, A.K., A.S., C.B. and J.B.; supervision, A.K., C.B. and J.B.; funding acquisition, A.S., C.B. and J.B. All authors have read and agreed to the published version of the manuscript.

Declaration of Competing Interest

Corresponding authors, on behalf of all the authors of a submission, disclose any financial and personal relationships with other people or organizations that could inappropriately influence our work. We declare no conflict of interest.

Data availability

Data will be made available on request.

References

[1] T. Aus der Beek, F.A. Weber, A. Bergmann, S. Hickmann, I. Ebert, A. Hein, A. Küster, Pharmaceuticals in the environment—global occurrences and perspectives, Environ. Toxicol. Chem. 35 (2016) 823–835, https://doi.org/10.1002/ETC.3339.

[2] Y. Zhang, S.R. Meshnick, Inhibition of plasmodium falciparum dihydropteroate synthetase and growth in vitro by sulfa drugs, Antimicrob. Agents Chemother. 35 (1991) 267–271, https://doi.org/10.1128/AAC.35.2.267.

[3] The Use of Drugs in Food Animals, Benefits and Risks, The Use of Drugs in Food Animals, 1999, https://doi.org/10.17226/5137.

[4] C. Borsetto, S. Raguideau, E. Travis, D.W. Kim, D.H. Lee, A. Bottrill, R. Stark, L. Song, C.J. Cha, J. Pearson, C. Quince, A.C. Singer, E.M.H. Wellington, Impact of sulfamethoxazole on a riverine microbiome, Water Res. 201 (2021), 117382, https://doi.org/10.1016/J.WATRES.2021.117382.

[5] C.R. dos Santos, Y.A.R. Lebron, V.R. Moreira, K. Koch, M.C.S. Amaral, Biodegradability, environmental risk assessment and ecological footprint in wastewater technologies for pharmaceutically active compounds removal, Bioresour. Technol. 343 (2022), 126150, https://doi.org/10.1016/J.BIORTECH.2021.126150.

[6] T. Thiebault, Sulfamethoxazole/trimethoprim ratio as a new marker in raw wastewaters: a critical review, Sci. Total Environ. 715 (2020), 136916, https://doi.org/10.1016/j.scitotenv.2020.136916.

[7] S. Rodriguez-Mozaz, S. Chamorro, E. Marti, B. Huerta, M. Gros, A. Sànchez-Melsió, C.M. Borrego, D. Barceló, J.L. Balcázar, Occurrence of antibiotics and antibiotic resistance genes in hospital and urban wastewaters and their impact on the receiving river, Water Res. 69 (2015) 234–242, https://doi.org/10.1016/j.watres.2014.11.021.

[8] X. Hu, Q. Zhou, Y. Luo, Occurrence and source analysis of typical veterinary antibiotics in manure, soil, vegetables and groundwater from organic vegetable bases, northern China, Environ. Pollut. 158 (2010) 2992–2998, https://doi.org/10.1016/j.envpol.2010.05.023.

[9] A. Christou, P. Karaolia, E. Hapeshi, C. Michael, D. Fatta-Kassinos, Long-term wastewater irrigation of vegetables in real agricultural systems: concentration of pharmaceuticals in soil, uptake and bioaccumulation in tomato fruits and human health risk assessment, Water Res. 109 (2017) 24–34, https://doi.org/10.1016/j.watres.2016.11.033.

[10] D. Azanu, B. Styrishave, G. Darko, J.J. Weisser, R.C. Abaidoo, Occurrence and risk assessment of antibiotics in water and lettuce in Ghana, Sci. Total Environ. 622–623 (2018) 293–305, https://doi.org/10.1016/j.scitotenv.2017.11.287.

[11] C.X. Chen, S.S. Yang, J. Ding, G.Y. Wang, L. Zhong, S.Y. Zhao, Y.N. Zang, J. Q. Jiang, L. Ding, Y. Zhao, L.M. Liu, N.Q. Ren, Non-covalent self-assembly synthesis of AQ2S@rGO nanocomposite for the degradation of sulfadiazine under solar irradiation: the indispensable effect of chloride, Appl. Catal. B. 298 (2021), 120495, https://doi.org/10.1016/J.APCATB.2021.120495.

[12] M.O. Alfred, M.O. Omorogie, O. Bodede, R. Moodley, A. Ogunlaja, O.G. Adeyemi, C. Günter, A. Taubert, I. Iermak, H. Eckert, I.D.A. Silva, A.S.S. de Camargo, A. de Jesus Motheo, S.M. Clarke, E.I. Unuabonah, Solar-active clay-TiO2 nanocomposites prepared via biomass assisted synthesis: efficient removal of ampicillin, sulfamethoxazole and artemether from water, Chem. Eng. J. 398 (2020), 125544, https://doi.org/10.1016/J.CEJ.2020.125544.

[13] S. Murgolo, C. de Ceglie, C. di Iaconi, G. Mascolo, Novel TiO2-based catalysts employed in photocatalysis and photoelectrocatalysis for effective degradation of pharmaceuticals (PhACs) in water: a short review, Curr. Opin. Green Sustain. Chem. 30 (2021), 100473, https://doi.org/10.1016/J.COGSC.2021.100473.

[14] A. Mirzaei, M. Eddah, S. Roualdes, D. Ma, M. Chaker, Multiple-homojunction gradient nitrogen doped TiO2 for photocatalytic degradation of sulfamethoxazole, degradation mechanism, and toxicity assessment, Chem. Eng. J. 422 (2021), 130507, https://doi.org/10.1016/J.CEJ.2021.130507.

[15] H. Anwer, J.W. Park, Lorentz force promoted charge separation in a hierarchical, bandgap tuned, and charge reversible NixMn(0.5−x)O photocatalyst for sulfamethoxazole degradation, Appl. Catal. B. 300 (2022), 120724, https://doi.org/10.1016/J.APCATB.2021.120724.

[16] P. Borthakur, P.K. Boruah, P. Das, M.R. Das, CuS nanoparticles decorated MoS2 sheets as an efficient nanozyme for selective detection and photocatalytic degradation of hydroquinone in water, New J. Chem. 45 (2021) 8714–8727, https://doi.org/10.1039/D1NJ00856K.

[17] Q. Chen, M. Zhang, J. Li, G. Zhang, Y. Xin, C. Chai, Construction of immobilized 0D/1D heterostructure photocatalyst au/CuS/CdS/TiO2 NBs with enhanced photocatalytic activity towards moxifloxacin degradation, Chem. Eng. J. 389 (2020), 124476, https://doi.org/10.1016/J.CEJ.2020.124476.

[18] Q. Chen, S. Wu, Y. Xin, Synthesis of Au–CuS–TiO2 nanobelts photocatalyst for efficient photocatalytic degradation of antibiotic oxytetracycline, Chem. Eng. J. 302 (2016) 377–387, https://doi.org/10.1016/J.CEJ.2016.05.076.

[19] C.J. Chang, W.C. Tsai, CuSZnS decorated Fe3O4 nanoparticles as magnetically separable composite photocatalysts with excellent hydrogen production activity, Int. J. Hydrog. Energy 44 (2019) 20872–20880, https://doi.org/10.1016/J.IJHYDENE.2018.06.083.

[20] C. Song, X. Wang, J. Zhang, X. Chen, C. Li, Enhanced performance of direct Z-scheme CuS-WO3 system towards photocatalytic decomposition of organic pollutants under visible light, Appl. Surf. Sci. 425 (2017) 788–795, https://doi.org/10.1016/J.APSUSC.2017.07.082.

[21] C. Lai, M. Zhang, B. Li, D. Huang, G. Zeng, L. Qin, X. Liu, H. Yi, M. Cheng, L. Li, Z. Chen, L. Chen, Fabrication of CuS/BiVO4 (0 4 0) binary heterojunction photocatalysts with enhanced photocatalytic activity for ciprofloxacin degradation and mechanism insight, Chem. Eng. J. 358 (2019) 891–902, https://doi.org/10.1016/J.CEJ.2018.10.072.

[22] M. Mokhtari Nesfchi, A. Ebrahimian Pirbazari, F.E. Khalil Saraei, F. Rojaee, F. Mahdavi, S.A. Fa'al Rastegar, Fabrication of plasmonic nanoparticles/cobalt doped TiO2 nanosheets for degradation of tetracycline and modeling the process by artificial intelligence techniques, Mater. Sci. Semicond. Process. 122 (2021), 105465, https://doi.org/10.1016/J.MSSP.2020.105465.

[23] G. Sadanandam, K. Lalitha, V.D. Kumari, M.V. Shankar, M. Subrahmanyam, Cobalt doped TiO2: a stable and efficient photocatalyst for continuous hydrogen production from glycerol: water mixtures under solar light irradiation, Int. J. Hydrog. Energy 38 (2013) 9655–9664, https://doi.org/10.1016/J.IJHYDENE.2013.05.116.

[24] S. Gu, A.N. Marianov, H. Xu, Y. Jiang, Effect of TiO2 support on immobilization of cobalt porphyrin for electrochemical CO2 reduction, J. Mater. Sci. Technol. 80 (2021) 20–27, https://doi.org/10.1016/J.JMST.2020.09.053.

[25] T.M.H. Nguyen, C.W. Bark, Synthesis of cobalt-doped TiO2 based on metal-organic frameworks as an effective Electron transport material in perovskite solar cells, ACS Omega. 5 (2020) 2280–2286, https://doi.org/10.1021/ACSOMEGA.9B03507/SUPPL_FILE/AO9B03507_SI_001.PDF.

[26] Z. Hosseinpour, S. Hosseinpour, M. Maaza, A. Scarpellini, Co2+ and Ho3+ doped CuS nanocrystals with improved photocatalytic activity under visible light irradiation, RSC Adv. 6 (2016) 42581–42588, https://doi.org/10.1039/C6RA03647C.

[27] J. Hou, B. Huang, L. Kong, Y. Xie, Y. Liu, M. Chen, Q. Wang, One-pot hydrothermal synthesis of CdS–CuS decorated TiO2 NTs for improved photocatalytic dye degradation and hydrogen production, Ceram. Int. 47 (2021) 30860–30868, https://doi.org/10.1016/J.CERAMINT.2021.07.268.

[28] X.L. Luo, Y.X. Yang, Z.L. Wang, S.Y. Yang, Y.H. Xu, CuS anchored onto peanut-like BiVO4 p-n heterojunction with enhanced photocatalytic degradation activity under visible light irradiation, Mater. Res. Bull. 156 (2022), 111985, https://doi.org/10.1016/J.MATERRESBULL.2022.111985.

[29] S. Brunauer, P.H. Emmett, E. Teller, Adsorption of gases in multimolecular layers, J. Am. Chem. Soc. 60 (2002) 309–319, https://doi.org/10.1021/JA01269A023.

[30] J. Tauc, Absorption edge and internal electric fields in amorphous semiconductors, Mater. Res. Bull. 5 (1970) 721–729, https://doi.org/10.1016/0025-5408(70)90112-1.

[31] M. Peñas-Garzón, A. Gómez-Avilés, M. Bedia, J.J. Rodriguez, C. Belver, Effect of activating agent on the properties of TiO2/activated carbon heterostructures for solar photocatalytic degradation of acetaminophen, Materials Vol. 12 (2019), https://doi.org/10.3390/MA12030378. Page 378. 12 (2019) 378.

[32] R.R. Solís, M. Peñas-Garzón, C. Belver, J.J. Rodriguez, J. Bedia, Highly stable UiO-66-NH2 by the microwave-assisted synthesis for solar photocatalytic water treatment, J. Environ. Chem Eng. 10 (2022), 107122, https://doi.org/10.1016/J.JECE.2021.107122.

[33] M. Peñas-Garzón, M.J. Sampaio, Y.L. Wang, J. Bedia, J.J. Rodriguez, C. Belver, C. G. Silva, J.L. Faria, Solar photocatalytic degradation of parabens using UiO-66-NH2, Sep. Purif. Technol. 286 (2022), 120467, https://doi.org/10.1016/J.SEPPUR.2022.120467.

[34] C. Baumanis, D.W. Bahnemann, TiO2 thin film electrodes: correlation between photocatalytic activity and electrochemical properties, J. Phys. Chem. C 112 (2008) 19097–19101, https://doi.org/10.1021/JP807655A.

[35] T. Giannakopoulou, I. Papailias, N. Todorova, N. Boukos, Y. Liu, J. Yu, C. Trapalis, Tailoring the energy band gap and edges' potentials of g-C3N4/TiO2 composite photocatalysts for NOx removal, Chem. Eng. J. 310 (2017) 571–580, https://doi.org/10.1016/J.CEJ.2015.12.102.

[36] G.P. Anipsitakis, D.D. Dionysiou, Degradation of organic contaminants in water with sulfate radicals generated by the conjunction of peroxymonosulfate with cobalt, Environ. Sci. Technol. 37 (2003) 4790–4797, https://doi.org/10.1021/ES0263792.

[37] G. Kresse, D. Joubert, From ultrasoft pseudopotentials to the projector augmented-wave method, Phys. Rev. B 59 (1999) 1758, https://doi.org/10.1103/PhysRevB.59.1758.

[38] J.P. Perdew, K. Burke, M. Ernzerhof, Generalized gradient approximation made simple, Phys. Rev. Lett. 77 (1996) 3865, https://doi.org/10.1103/PhysRevLett.77.3865.

[39] S. Grimme, Semiempirical GGA-type density functional constructed with a long-range dispersion correction, J. Comput. Chem. 27 (2006) 1787–1799, https://doi.org/10.1002/JCC.20495.

[40] J. Ludwig, L. An, B. Pattengale, Q. Kong, X. Zhang, P. Xi, J. Huang, Ultrafast hole trapping and relaxation dynamics in p-type CuS nanodisks, J. Phys. Chem. Lett. 6 (2015) 2671–2675, https://doi.org/10.1021/ACS.JPCLETT.5B01078/SUPPL_FILE/JZ5B01078_SI_001.PDF.

[41] C. Beynis, Indium insertions in non-stoichiometric copper sulfides, CuxS, and their effect on the localized surface plasmon resonance of the nanocrystals, Appl. Phys. A Mater. Sci. Process. 125 (2019) 1–8, https://doi.org/10.1007/S00339-019-2546-4/FIGURES/7.

[42] B. Yu, F. Meng, T. Zhou, A. Fan, M.W. Khan, H. Wu, X. Liu, Construction of hollow TiO$_2$/CuS nanoboxes for boosting full-spectrum driven photocatalytic hydrogen evolution and environmental remediation, Ceram. Int. 47 (2021) 8849–8858, https://doi.org/10.1016/J.CERAMINT.2020.12.006.

[43] Z. Huang, L. Wang, H. Wu, H. Hu, H. Lin, L. Qin, Q. Li, Shape-controlled synthesis of CuS as a Fenton-like photocatalyst with high catalytic performance and stability, J. Alloys Compd. 896 (2022), 163045, https://doi.org/10.1016/J.JALLCOM.2021.163045.

[44] G. Nabi, M. Tanveer, M. Bilal Tahir, M. Kiran, M. Rafique, N.R. Khalid, M. Alzaid, N. Fatima, T. Nawaz, Mixed solvent based surface modification of CuS nanostructures for an excellent photocatalytic application, Inorg. Chem. Commun. 121 (2020), 108205, https://doi.org/10.1016/J.INOCHE.2020.108205.

[45] Z. Wu, X. Liu, C. Yu, F. Li, W. Zhou, L. Wei, Construct interesting CuS/TiO$_2$ architectures for effective removal of Cr(VI) in simulated wastewater via the strong synergistic adsorption and photocatalytic process, Sci. Total Environ. 796 (2021), 148941, https://doi.org/10.1016/J.SCITOTENV.2021.148941.

[46] Y.Y. Lu, Y.Y. Zhang, J. Zhang, Y. Shi, Z. Li, Z.C. Feng, C. Li, In situ loading of CuS nanoflowers on rutile TiO$_2$ surface and their improved photocatalytic performance, Appl. Surf. Sci. 370 (2016) 312–319, https://doi.org/10.1016/J.APSUSC.2016.02.170.

[47] R.G. Toro, M. Diab, T. de Caro, M. Al-Shemy, A. Adel, D. Caschera, Study of the effect of titanium dioxide hydrosol on the photocatalytic and mechanical properties of paper sheets, Materials 13 (2020), https://doi.org/10.3390/MA13061326. Page 1326. 13 (2020) 1326.

[48] K.M. Reddy, S.V. Manorama, A.R. Reddy, Bandgap studies on anatase titanium dioxide nanoparticles, Mater. Chem. Phys. 78 (2003) 239–245, https://doi.org/10.1016/S0254-0584(02)00343-7.

[49] M. Nowak, B. Kauch, P. Szperlich, Determination of energy band gap of nanocrystalline SbSI using diffuse reflectance spectroscopy, Rev. Sci. Instrum. 80 (2009), 046107, https://doi.org/10.1063/1.3103603.

[50] S. Jia, X. Li, B. Zhang, J. Wang, J. Yang, S. Zhang, S. Li, Z. Zhang, TiO$_2$/CuS heterostructure nanowire array photoanodes toward water oxidation: the role of CuS, Appl. Surf. Sci. 463 (2019) 829–837, https://doi.org/10.1016/J.APSUSC.2018.09.003.

[51] O. Carp, C.L. Huisman, A. Reller, Photoinduced reactivity of titanium dioxide, Prog. Solid State Chem. 32 (2004) 33–177, https://doi.org/10.1016/J.PROGSOLIDSTCHEM.2004.08.001.

[52] R. Katal, S.M. Panah, M. Zarinejad, M. Salehi, H. Jiangyong, Synthesis of self-gravity settling faceted-anatase TiO$_2$ with dominant {010} facets for the photocatalytic degradation of acetaminophen and study of the type of generated oxygen vacancy in faceted-TiO2, Water 10 (2018), https://doi.org/10.3390/W10101462. Page 1462. 10 (2018) 1462.

[53] S. Sarkar, C. Bhattacharjee, S. Curcio, Studies on adsorption, reaction mechanisms and kinetics for photocatalytic degradation of CHD, a pharmaceutical waste, Ecotoxicol. Environ. Saf. 121 (2015) 154–163, https://doi.org/10.1016/J.ECOENV.2015.04.036.

[54] W. Wei, H. Gong, L. Sheng, H. Wu, S. Zhu, L. Feng, X. Li, W. You, Highly efficient photocatalytic activity and mechanism of novel Er^{3+} and Tb^{3+} co-doped BiOBr/g-C$_3$N$_5$ towards sulfamethoxazole degradation, Ceram. Int. 47 (2021) 24062–24072, https://doi.org/10.1016/J.CERAMINT.2021.05.116.

[55] H. Diarmand-Khalilabad, A. Habibi-Yangjeh, D. Seifzadeh, S. Asadzadeh-Khaneghah, E. Vesali-Kermani, G-C$_3$N$_4$ nanosheets decorated with carbon dots and CdS nanoparticles: novel nanocomposites with excellent nitrogen photofixation ability under simulated solar irradiation, Ceram. Int. 45 (2019) 2542–2555, https://doi.org/10.1016/J.CERAMINT.2018.10.185.

[56] R.R. Solís, A. Gómez-Avilés, C. Belver, J.J. Rodriguez, J. Bedia, Microwave-assisted synthesis of NH$_2$-MIL-125(Ti) for the solar photocatalytic degradation of aqueous emerging pollutants in batch and continuous tests, J. Environ. Chem Eng. 9 (2021), 106230, https://doi.org/10.1016/J.JECE.2021.106230.

[57] P. Kar, S. Farsinezhad, X. Zhang, K. Shankar, Anodic Cu2S and CuS nanorod and nanowall arrays: preparation, properties and application in CO$_2$ photoreduction, Nanoscale. 6 (2014) 14305–14318, https://doi.org/10.1039/C4NR05371K.

[58] E.M. Sitinjak, I. Masmur, N.V.M.D. Marbun, P.E. Hutajulu, G. Gultom, Y. Sitanggang, Direct Z-scheme of n-type CuS/p-type ZnS@electrospun PVP nanofiber for the highly efficient catalytic reduction of 4-nitrophenol and mixed dyes, RSC Adv. 12 (2022) 16165–16173, https://doi.org/10.1039/D2RA01476A.

[59] J. Liu, J. Feng, J. Gui, T. Chen, M. Xu, H. Wang, H. Dong, H. Chen, X. Li, L. Wang, Z. Chen, Z. Yang, J. Liu, W. Hao, Y. Yao, L. Gu, Y. Weng, Y. Huang, X. Duan, J. Zhang, Y. Li, Metal@semiconductor core-shell nanocrystals with atomically organized interfaces for efficient hot electron-mediated photocatalysis, Nano Energy 48 (2018) 44–52, https://doi.org/10.1016/J.NANOEN.2018.02.040.

[60] A. el Mragui, O. Zegaoui, J.C.G. Esteves da Silva, Elucidation of the photocatalytic degradation mechanism of an azo dye under visible light in the presence of cobalt doped TiO$_2$ nanomaterials, Chemosphere. 266 (2021), 128931, https://doi.org/10.1016/J.CHEMOSPHERE.2020.128931.

[61] Y. Zhang, W. Chu, Cooperation of multi-walled carbon nanotubes and cobalt doped TiO$_2$ to activate peroxymonosulfate for antipyrine photocatalytic degradation, Sep. Purif. Technol. 282 (2022), 119996, https://doi.org/10.1016/J.SEPPUR.2021.119996.

[62] W. Zhu, Z. Li, C. He, S. Faqian, Y. Zhou, Enhanced photodegradation of sulfamethoxazole by a novel WO$_3$-CNT composite under visible light irradiation, J. Alloys Compd. 754 (2018) 153–162, https://doi.org/10.1016/J.JALLCOM.2018.04.286.

[63] Á. Morales-García, J. He, A.L. Soares, H.A. Duarte, Surfaces and morphologies of covellite (CuS) nanoparticles by means of ab initio atomistic thermodynamics, CrystEngComm. 19 (2017) 3078–3084, https://doi.org/10.1039/C7CE00203C.

[64] A. Slassi, P.B. Sorokin, A. Pershin, Ohmic/Schottky barrier engineering in metal/SnP$_3$ heterostructures, J. Alloys Compd. 831 (2020), 154800, https://doi.org/10.1016/J.JALLCOM.2020.154800.

[65] A. Slassi, J. Cornil, Theoretical characterization of strain and interfacial electronic effects in donor-acceptor bilayers of 2D transition metal dichalcogenides, 2d Mater. 6 (2018), 015025, https://doi.org/10.1088/2053-1583/AAF1D4.

[66] J. Zhang, X. Chen, Y. Bai, C. Li, Y. Gao, R. Li, C. Li, Boosting photocatalytic water splitting by tuning built-in electric field at phase junction, J. Mater. Chem. A Mater. 7 (2019) 10264–10272, https://doi.org/10.1039/C8TA08199A.

[67] J. Li, A. Slassi, X. Han, D. Cornil, M.H. Ha-Thi, T. Pino, D.P. Debecker, C. Colbeau-Justin, J. Arbiol, J. Cornil, M.N. Ghazzal, Tuning the electronic bandgap of graphdiyne by H-substitution to promote interfacial charge carrier separation for enhanced photocatalytic hydrogen production, Adv. Funct. Mater. 31 (2021) 2100994, https://doi.org/10.1002/ADFM.202100994.

[68] E. Zojer, T.C. Taucher, O.T. Hofmann, The impact of dipolar layers on the electronic properties of organic/inorganic hybrid interfaces, Adv. Mater. Interfaces 6 (2019) 1900581, https://doi.org/10.1002/ADMI.201900581.

[69] D. Cornil, T. van Regemorter, D. Beljonne, J. Cornil, Work function shifts of a zinc oxide surface upon deposition of self-assembled monolayers: a theoretical insight, Phys. Chem. Chem. Phys. 16 (2014) 20887–20899, https://doi.org/10.1039/C4CP02811B.